Formation mechanisms and optimization of trap-based positron beams

Cite as: Phys. Plasmas **23**, 023505 (2016); https://doi.org/10.1063/1.4942034 Submitted: 05 November 2015 . Accepted: 03 February 2016 . Published Online: 16 February 2016

M. R. Natisin, J. R. Danielson, and C. M. Surko







ARTICLES YOU MAY BE INTERESTED IN

Formation of buffer-gas-trap based positron beams
Physics of Plasmas 22, 033501 (2015); https://doi.org/10.1063/1.4913354

A cryogenically cooled, ultra-high-energy-resolution, trap-based positron beam Applied Physics Letters 108, 024102 (2016); https://doi.org/10.1063/1.4939854

Magnetic field extraction of trap-based electron beams using a high-permeability grid Physics of Plasmas 22, 073503 (2015); https://doi.org/10.1063/1.4923460







Formation mechanisms and optimization of trap-based positron beams

M. R. Natisin, ^{a)} J. R. Danielson, and C. M. Surko Department of Physics, University of California, San Diego, La Jolla, California 92093, USA

(Received 5 November 2015; accepted 3 February 2016; published online 16 February 2016)

Described here are simulations of pulsed, magnetically guided positron beams formed by ejection from Penning-Malmberg-style traps. In a previous paper [M. R. Natisin et al., Phys. Plasmas 22, 033501 (2015)], simulations were developed and used to describe the operation of an existing trap-based beam system and provided good agreement with experimental measurements. These techniques are used here to study the processes underlying beam formation in more detail and under more general conditions, therefore further optimizing system design. The focus is on lowenergy beams (~eV) with the lowest possible spread in energies (<10 meV), while maintaining microsecond pulse durations. The simulations begin with positrons trapped within a potential well and subsequently ejected by raising the bottom of the trapping well, forcing the particles over an end-gate potential barrier. Under typical conditions, the beam formation process is intrinsically dynamical, with the positron dynamics near the well lip, just before ejection, particularly crucial to setting beam quality. In addition to an investigation of the effects of beam formation on beam quality under typical conditions, two other regimes are discussed; one occurring at low positron temperatures in which significantly lower energy and temporal spreads may be obtained, and a second in cases where the positrons are ejected on time scales significantly faster than the axial bounce time, which results in the ejection process being essentially non-dynamical. © 2016 AIP Publishing LLC. [http://dx.doi.org/10.1063/1.4942034]

I. INTRODUCTION

Positron interactions with ordinary matter are important in a variety of contexts, including atomic physics, material science, astrophysics, and medicine.^{1–4} The primary method of studying such interactions is to direct a low energy positron beam into a target material (e.g., an atomic or molecular gas, a solid, or solid surface) and to measure the properties of the scattered positron or, in the case of annihilation, use the emitted gamma radiation as a measure of the underlying interaction. For such measurements, the accuracy with which these interactions can be studied is frequently set by the spread (either energy or time) of the positron beam used to probe them.

Trap-based antiparticle beams have been produced using a variety of techniques, with the primary distinctions pertaining to the methods used to cool the particles and the manner in which the beam is generated. Sympathetic, cyclotron cooling on electrons and auto-resonant ejection has been used to create cold antiproton beams from an antiproton plasma.⁵ Also working in the plasma regime, methods to extract cyclotron-particles from single-component plasmas have been developed, both as a magnetically guided beam, ^{6,7} and later, extracted from the magnetic field to create an electrostatic beam.^{8,9} The focus here is the creation of a magnetically guided low-energy positron beam. The primary method of producing these beams is using a so-called buffer-gas trap (BGT), in which positrons in the single-particle regime are cooled through interactions with a molecular gas and subsequently ejected as a pulsed beam. 10,11

The BGT is capable of producing pulsed, magnetically guided positron beams tunable from 0.1 eV to keV energies. These devices are now used in a wide variety of applications, including antihydrogen, ^{12–15} formation of dense gases of positronium atoms, ¹⁶ material science, ¹⁷ and atomic physics studies. ^{1,18} Using these techniques, positron beams with tens of milli-electron volt energy spreads or sub-microsecond temporal spreads are routinely produced. ^{11,19} Although these beam characteristics are sufficient for probing well-isolated processes at energies ≥50 meV, many other processes are difficult or impossible to study without further advances in beam technology.

Presented here are simulation results of trap-based positron beams formed using a variety of trap geometries and ejection conditions. The simulation technique was discussed previously for the case where the parameters were chosen specifically to replicate experimental conditions, thus allowing direct comparisons with measurements of beam properties. Frequent reference is made to this previous work, hereafter labeled Ref. I, as many considerations and formulae relevant here will not be repeated in the interest of brevity. While Ref. I provided new insights into the underlying physical processes and validated the simulations, the work presented here uses the simulations to explore a larger parameter space not constrained by existing hardware.

The goal of this paper is to develop a deeper understanding of the underlying physical phenomena operative during beam formation and to provide a practical guide for optimization of next-generation, low-energy-spread, positron beams. Of key importance is the identification of three distinct regimes under which beam formation may occur. Besides the regime in which current traps typically operate,

a) Author to whom correspondence should be addressed. Electronic mail: mnatisin@physics.ucsd.edu

there exists a regime at low positron temperatures in which the possible positron trajectories become constrained, resulting in significant improvements to both energy and temporal spreads. Finally, a third regime is described in which the positrons are ejected on time scales significantly faster than their initial axial bounce time, resulting in the beam formation process becoming essentially non-dynamic. Important beam-formation parameters investigated include the voltage ramp rate with which the trapping well is raised to release the particles, the positron temperature, the trapping potential, and the electrode geometry. Optimized choices and/or tradeoffs for these parameters are discussed.

The paper begins in Sec. II with a brief overview of the simulation, followed by a description of the generic Penning-Malmberg (PM) style trap and ejection protocols used throughout the paper. Section III describes how the various beam distributions are characterized, while Sec. IV describes the dynamic processes encountered during beam formation in the three regimes discussed here. Simulation results, along with discussions regarding the underlying physics, are presented in Sec. V for a variety of ejection conditions and trapping geometries. The paper ends with a set of concluding remarks in Sec. VI.

II. DESCRIPTION OF THE SIMULATION

A. Simulation details

The details of the simulation are described in Ref. I. The simulation is of Monte-Carlo-type and follows the trajectory of a large number of particles (typically $\sim 10^4$) through time-dependent potentials and static magnetic fields. It assumes cylindrical symmetry and neglects space-charge, positron-positron, and positron-neutral effects (i.e., the positrons are in the single-particle regime and beam formation times are assumed fast compared to collision times). The externally applied potentials are allowed to vary axially, radially, and temporally, while the magnetic field B is held constant here in order to more clearly examine the effects of the beam formation process on the resulting beam. The effects of varying B axially are discussed in Ref. I.

The axial positions and parallel velocities are calculated as the particle moves along a magnetic field line by numerically integrating the equations of motion as described in Ref. I. For a positively charged particle with charge e in a potential ϕ and constant magnetic field B, the parallel force is

$$F_{\parallel}(z,r,t) = -e\frac{d\phi(z,r,t)}{dz},\tag{1}$$

where z is along the direction of the magnetic field.

The perpendicular velocity v_{\perp} and radial coordinate of the guiding center r remain constant during the formation and propagation of the beam due to the constant B and the adiabatic invariance of the positron magnetic moment

$$\mu = \frac{mv_{\perp}^2}{2B}.\tag{2}$$

The externally applied potentials are first calculated as a function of z, r, and t on a grid of 0.05 cm, 0.25 cm, and 1 ns,

respectively, using a finite-element method with the specified electrode geometry. A more precise value of $\phi(z,r,t)$ is then obtained by interpolating the grid solutions at the specific z and r positions calculated from the numerical integration at a given t. This last step is particularly important for simulating some of the narrower potential well geometries considered here. For the numerical integration, a time step δt of 1 ns was used. Reducing this time step by an order of magnitude had no significant effect on the results.

As stated above, these simulation results assume that the effects of space-charge and positron-neutral collisions are negligible. Experimental measurements show that the measured beam-energy distributions are relatively insensitive to positron number, at least until the space-charge potential becomes comparable to or larger than the parallel energy spread of the beam. The simulation results of the beam-energy distributions presented in Ref. I, for example, are in good agreement with experimental measurements. In contrast, measurements show that the beam temporal distribution is relatively sensitive to positron number, with the temporal spread increasing with increasing positron number. The effects of positron-neutral collisions are discussed below, where appropriate.

B. The generic PM trap

An example of the generic trap geometry and confinement potentials is shown in Fig. 1. This is arguably the simplest possible PM trap, consisting of three cylindrically symmetric electrodes labeled from left to right as the trapping, well, and exit-gate electrodes with corresponding applied voltages V_T , V_W , and V_E . Voltages V_T and V_E provide axial confinement and are held constant, with $V_E < V_T$ to give a directionality to the ejected beam. The initial well voltage $V_W(0)$ then determines the initial well depth $V_E - V_W(0)$.

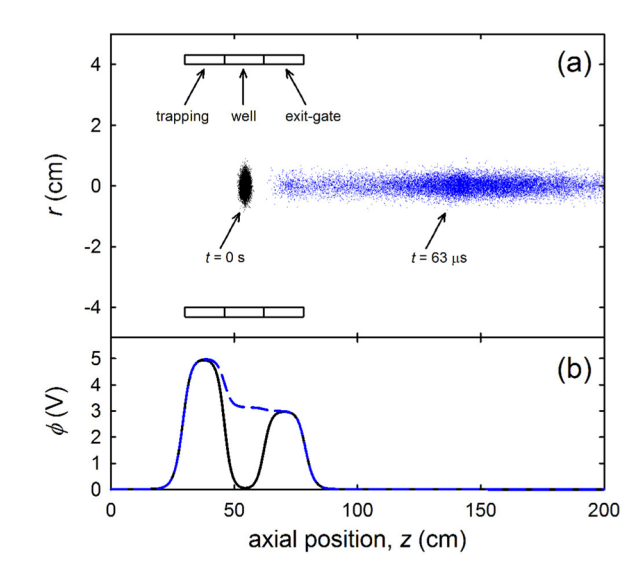


FIG. 1. (a) Electrode geometry showing the axial and radial positions of the particles during a typical beam pulse, and (b) the on-axis potential at (black) $t=0~\mu s$ and (blue) $t=63~\mu s$. The voltages applied to the trapping and exitgate electrodes are 5 V and 3 V, with the well voltage increased linearly from 0 V at $t=0~\mu s$ at a rate of $50~\text{mV}/\mu s$. All electrodes have lengths of L=16~cm and aspect ratios of $\alpha=2$.

The trap geometry is specified by the electrode lengths L and aspect ratios $\alpha \equiv L/D$, where D is the electrode inner diameter. The electrode length sets the overall length of the potential barrier (or well) provided by the electrode, while its aspect ratio determines the shape. Electrodes with small aspect ratio provide less uniform, more parabolic potentials, while large aspect ratio electrodes produce potentials with flat regions near their center in the axial direction.

As seen in Fig. 1, the particles are initially placed within the potential well with the initial parallel and perpendicular velocity distributions chosen to be 1-D and 2-D Maxwell-Boltzmann (MB) distributions at a given temperature, and the initial radial positions Gaussian distributed with a full-width at half-max (FWHM) of 0.5 cm. The pulse is then formed by increasing the voltage applied to the well electrode according to a specified ramp function until the particles are lifted over the exit-gate potential and ejected from the trap.

III. CHARACTERIZATION OF BEAM DISTRIBUTIONS

The focus of this study is on the energy and time distributions of the beam pulses. Narrow total energy distributions allow for more precise probing of physical processes, such as measurement of scattering cross sections or study of resonances in positron annihilation, while narrow time distributions allow for precise timing, thus providing better discrimination against extrinsic noise.

The total energy distribution can be decomposed into two components; one for motion parallel to B and another in the cyclotron motion perpendicular to B. As discussed in Ref. I, the parallel energy distribution is largely set by the beam formation processes, while the perpendicular distribution is independent of how the beam was formed and depends only on the initial positron temperature and B(z). As discussed above, here B is held constant along z, and so the perpendicular energy distribution remains constant throughout beam formation and propagation.

As discussed in detail in Ref. I, under typical conditions the parallel energy and time distributions can be approximated as Gaussians, while the perpendicular energy distribution is (2D) Maxwell-Boltzmann. The total energy distribution is a convolution of both, resulting in a so-called exponentially modified Gaussian (EMG) distribution. ^{20,21} Conditions under which the parallel distribution deviates significantly from a Gaussian are described at the end of Sec. V.

The spreads in the distributions are quantified here by their standard deviations. Since the total energy of a given positron is the sum of its parallel and perpendicular energies, the standard deviation of the total energy distribution σ_t may be written as

$$\sigma_t = \sqrt{\sigma_{\parallel}^2 + \sigma_{\perp}^2},\tag{3}$$

where σ_{\parallel} and σ_{\perp} are the standard deviations of the parallel and perpendicular distributions. This shows that the total energy spread is sensitively limited by the largest component. Significant reductions to σ_{\perp} , for example, will only improve the total energy spread until $\sigma_{\perp} \ll \sigma_{\parallel}$, at which point

 σ_{\parallel} will dominate. For this reason, optimizing beam energy spread requires reducing *both* σ_{\parallel} and σ_{\perp} .

IV. DYNAMICS OF BEAM FORMATION

As described in Ref. I, the beam formation process under typical conditions is highly dynamic in nature, with each particle following a unique trajectory through phasespace as it interacts with the changing potential. The particles bounce in the well with a frequency that depends on the shape of the trapping potential as the well voltage V_W is increased at a rate \dot{V}_W . As V_W is increased, the well width increases and the curvature of the potential decreases, leading to an increase in the particle bounce time and a decrease in the parallel temperature of the particles due to adiabatic cooling. Particles are first able to escape the trap only when they have sufficient kinetic plus potential energy to overcome the exit-gate barrier, which may occur at any point during the final bounce cycle depending upon the initial particle energy and phase of oscillation in the well.

In this paper, three distinct regimes for beam formation are discussed. The regime in which most BGTs currently operate is termed here the "full bounce" regime. Additionally, a new regime is identified which allows for significantly better beam quality to be obtained. Termed the "low temperature" regime, this occurs when the positron temperature is low enough to constrain the possible positron trajectories and therefore minimize the energy and time spreads of the resulting beam. Finally, there exists a third regime in which the positrons are ejected from the well on time scales significantly faster than the initial axial bounce time. In this "nondynamic" regime, the beam formation processes are vastly simplified and under certain conditions may provide superior beam energy spreads. The unique dynamics governing beam formation in each of these three regimes are introduced below.

In order to more clearly display the effects of beam formation on beam quality, the trajectories of the particles with the lowest and highest final parallel energies in the resulting beam, thus setting the *full* width of the parallel energy distribution, are shown in Fig. 2 for typical conditions in each of the three regimes. Also shown are the on-axis potentials and corresponding particle positions at five evenly divided times during the time the particles are able to escape the trap. This interval begins when the first particle has kinetic plus potential energy greater than the maximum in the exit-gate potential at this time, ϕ_E , and ends when the final particle crosses the position of the peak in the exit-gate potential, z_E .

While only the extreme trajectories are shown in Fig. 2, the beam is the result of the unique trajectories of many thousands of particles. The change in parallel energy during beam formation of a given particle may be described using a basic feature of Hamiltonian systems, namely, that for the Hamiltonian H(z, t) of a particle in an electrostatic potential $dH/dt = (\partial H/\partial t)_z$. Additionally, since the particle is unable to escape the trap until $E_0 + \delta E_{\parallel} > e\phi_E$, where E_0 is its initial kinetic plus potential energy and δE_{\parallel} is its change in parallel energy during beam formation, it is useful to write the

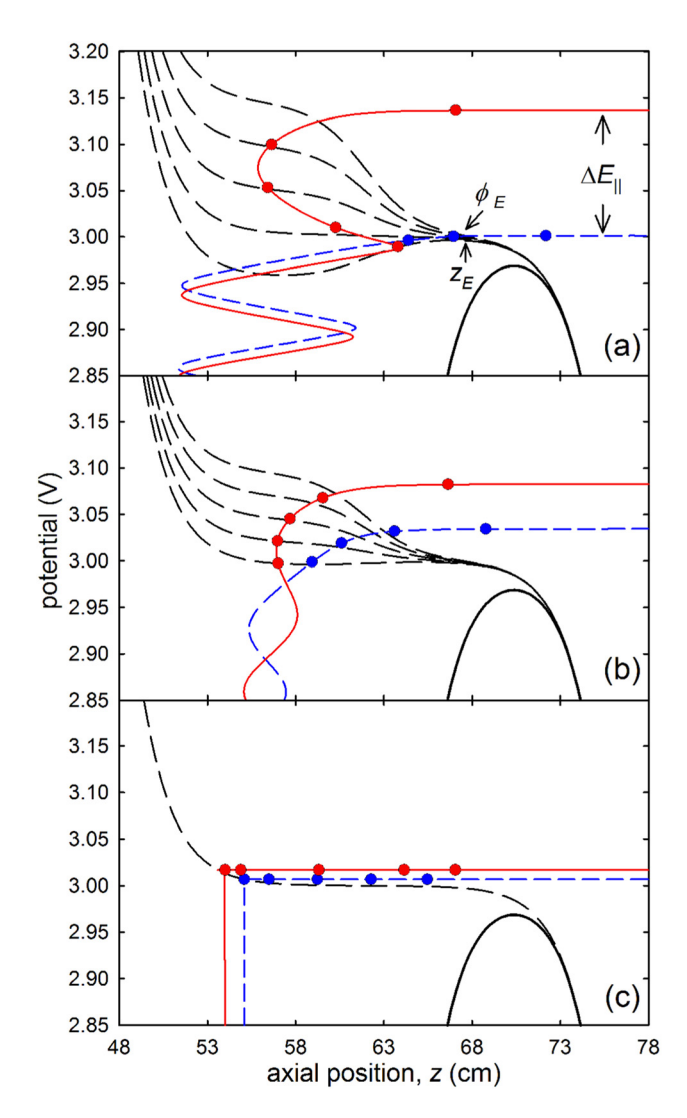


FIG. 2. (a) (—) Initial on-axis potential and trajectories of the particles with the (– –) lowest and (—) highest final parallel energies in the resulting beam, thus setting the full width of the parallel energy distribution ΔE_{\parallel} . (– –) and (\blacksquare) show potentials and particle positions at 5 evenly divided times during ejection; (a) full bounce regime: $T_0 = 300\,\mathrm{k}$, (b) low temperature regime: $T_0 = 10\,\mathrm{K}$, and (c) non-dynamic regime: $T_0 = 10\,\mathrm{K}$ and well voltage increased linearly from 0 to 3 V in 10 ns. All other parameters as in Fig. 1.

final parallel energy of a given particle in the resulting beam as

$$E_{\parallel} = e\phi_E + \int_{t_U}^{t_E} \left[\frac{\partial \phi(z, t)}{\partial t} \right]_z dt. \tag{4}$$

Here, t_U is the time at which the particle energy equals $e\phi_E$ and therefore becomes "untrapped," and t_E is the time at which it crosses the position of the peak in the exit-gate potential z_E (beyond which $\partial \phi/\partial t \approx 0$), and thus is ejected from the trap.

A key feature seen in the full bounce regime (Fig. 2(a)) is that the fate of the particles in and following their final bounce in the well fixes the spread of energies and times in the resulting beam. The lowest energy particle in the beam, which is among the first to escape the trap, is the one which obtains sufficient energy to overcome the exit-gate barrier at the *end* of a bounce cycle ($t_U \approx t_E$ in Eq. (4)), where a

bounce cycle is defined to begin and end upon reflection from the exit-gate barrier, thus releasing it with the minimum possible energy $E_{\parallel} \sim e\phi_E$. In contrast, the particle ejected with the highest parallel energy, which is among the last to escape the trap, is the one which encounters the barrier with an energy slightly less than necessary to escape. In this case, the particle is reflected such that it gains sufficient energy to escape the trap at the *beginning* of its next bounce cycle, but is forced to make another full pass through the rising potential region before escaping $(t_E - t_U \approx \tau_f^h)$, where τ_f^h is the time required for this particle to make its final transit through the rising potential region). Therefore, the highest energy particle is ejected with the maximum possible energy, $E_{\parallel} \sim e\phi_E + \tau_f^h\dot{V}_W$.

In contrast, at low temperatures where the initial phasespace is significantly reduced, the particles bounce within only a small region of the potential well and are therefore unable to escape the trap until $V_W \approx e\phi_E$ and the potential is nearly flat (Fig. 2(b)). This results in a majority of the particles obtaining sufficient energy to escape the trap at the same time, but still having to traverse a significant portion of the rising potential region before being ejected. Because of this, all particles are lifted above the exit-gate potential before being ejected (there is no trajectory for which $T_U \approx T_E$ in Eq. (4)), and no particles are able to gain sufficient energy to escape at the beginning of a bounce cycle (there is no trajectory for which $T_E - T_U \approx \tau_f^h$). In this low temperature regime, particles that are ejected with the lowest (highest) parallel energies are those that have the largest parallel energy and are traveling towards (away from) the exitgate barrier at the time they have sufficient energy to escape.

Finally, an example of the trajectories obtained in the non-dynamic regime is shown in Fig. 2(c). Here, it is seen that the well potential is raised sufficiently fast that the axial motion of the particles is negligible during this time, and therefore the complicated dynamic processes encountered in the other two regimes are absent. Specifically, adiabatic cooling does not occur and the initial parallel energy distribution is unaltered by the presence of the exit-gate barrier. Further, provided the final potential is reasonably flat over the region the particles occupy, particles will simply be ejected from the trap with their initial thermal energies plus their potential relative to ground. Under these conditions, the parallel energy distribution is a shifted Maxwell-Boltzmann distribution with $\sigma_{\parallel} = 1/2k_bT_0$, while the perpendicular energy distribution remains MB distributed with $\sigma_{\perp} = k_b T_0$ (as is the case in all of the regimes discussed here). Using Eq. (3), the total energy spread may then simply be written as $\sigma_t = \sqrt{5/2k_bT_0}$. Note that an alternate method of obtaining this result would be to rapidly drop the exit-gate barrier rather than increase the potential well, however in the interest of brevity only the case of increasing the potential well is considered here.

As will be shown, each of the three regimes described above has unique advantages and disadvantages for a given application. For example, the full bounce regime does not require special hardware; however, beam performance in this regime is limited. In contrast, the low temperature regime provides significantly improved energy and temporal spreads compared with the full bounce regime, but requires the particles to be cooled to low temperatures before ejection. In the non-dynamic regime, the processes undergone during beam formation are simplified, and the strong temperature dependence of the energy distributions provides excellent energy spreads at low temperatures; however, this regime requires the most sophisticated hardware and typically yields broader temporal spreads than the other two regimes.

V. SIMULATION RESULTS

As discussed above, the simulations reported here are done in a uniform magnetic field, and so the spread in perpendicular energy is constant everywhere with $\sigma_{\perp} = k_b T_0$, where k_b is Boltzmann's constant and T_0 is the particle initial temperature. Under these conditions, the total energy distribution varies only with σ_{\parallel} and may be obtained using Eq. (3). For this reason, only the affects of beam formation on σ_{\parallel} and σ_{τ} are discussed here.

A. Dependence on ejection protocol

Here, the initial well geometry is held fixed and the time-dependence of the applied well voltage, $V_W(t)$, is varied. The particle ejection rate is quantified by the ejection ramp rate, \dot{V}_W , which represents the *average* rate of change in the voltage applied to the well electrode during the time the particles are leaving the trap. The ramp rate is obtained by evaluating the derivative of the ramp function at the time each particle crosses the peak in the exit-gate potential, and taking the average.

Shown in Figs. 3(a) and 3(b) are the standard deviations of the energy and time distributions as a function of their calculated average ramp rates for beams generated using three distinct protocols for varying the particle ejection rate, with all other parameters as in Fig. 1. Here, it is seen that at a given ramp rate, the same value for both σ_{\parallel} and σ_{τ} is obtained regardless of the protocol used to eject the beam, indicating that the ejection rate as the particles are raised above the end-gate potential, V_W , is the important quantity and not the time dependence of $V_W(t)$ at earlier times. This simplifies greatly parameterization of the dynamic aspects of the beam formation process, allowing the ejection process to be well described by the single parameter V_W . Thus, in the remainder of this paper a linear ramp (i.e., V_W held fixed) is used to eject the particles, allowing other parameters to be more clearly examined.

As seen in Fig. 3, increasing \dot{V}_W leads to an increase in σ_{\parallel} and a decrease in σ_{τ} . This occurs because at higher ramp rates the particles are given more energy during their final pass through the rising potential region and are accelerated out of the trap more quickly due to the increased electric field, respectively. Of particular significance, as shown in Fig. 3(c), is that the ratio $\sigma_{\parallel}/\sigma_{\tau}$ varies linearly with \dot{V}_W with a coefficient of order unity; namely,

$$\sigma_{\parallel} = \beta \dot{V}_W \sigma_{\tau},\tag{5}$$

where $\beta \approx 1.5$. This equation, which derives from the principle encapsulated in Eq. (4), may be understood by examining

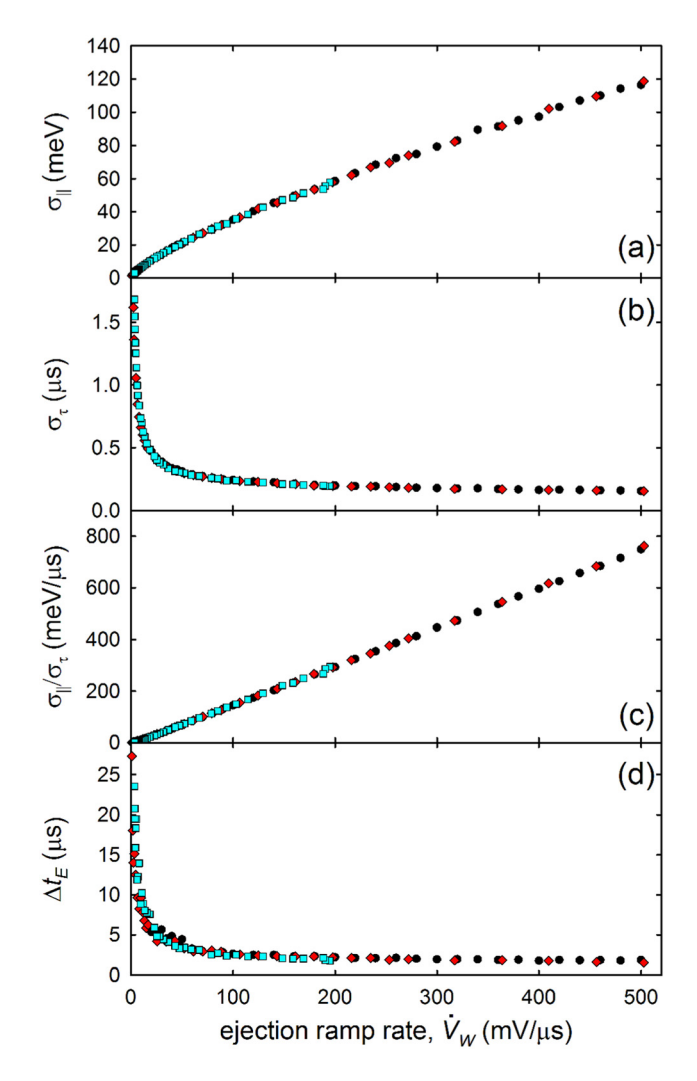


FIG. 3. Standard deviations of the (a) parallel energy and (b) time distributions, shown as a function of the calculated average ramp rates during the time particles escaped the trap. Also shown is the (c) ratio of the energy and temporal distributions and (d) total ejection time. Beams were generated using (\bullet) a linear ramp with \dot{V}_W varied from 20 to 500 mV/ μ s, (\bullet) an RC ramp with the final voltage varied from 3.0 to 9.0 V and e-fold time fixed at 10 μ s, and (\blacksquare) an RC ramp with e-fold time varied from 1 to 140 μ s and final voltage fixed at 3.5 V. All other parameters as in Fig. 1.

how the energy and temporal spreads are affected by the total time required to eject all particles.

The effect of the ramp rate on the total ejection time Δt_E is shown in Fig. 3(d), where the Δt_E is defined as the time between the first and last particle crossing the peak in the exit-gate potential and therefore escaping the trap. Comparing Figs. 3(c) and 3(d), it is seen that $\sigma_{\tau} \propto \Delta t_E$. Further, under these conditions the parallel energy spread is primarily set by the rising potential, and so $\sigma_{\parallel} \propto \Delta t_E \dot{V}_W$. As \dot{V}_W is increased, Δt_E decreases, resulting in a decrease in temporal spread. However, the product $\Delta t_E \dot{V}_W$ increases, leading to an increase in σ_{\parallel} . These two relationships result in a coupling of the parallel energy and temporal spreads via the ramp rate, as described by Eq. (5).

Note that under the conditions shown here, beam formation is in the full bounce regime; however, simulations in the low temperature regime (discussed below) result in the same dependence on \dot{V}_W shown in Fig. 3, with both σ_{\parallel} and σ_{τ}

reduced by a constant numerical scale factor which depends on the particle temperature. It should also be noted that in the non-dynamic regime $\dot{V}_W \approx 0$ since the potential is no longer changing by the time the positrons are ejected from the trap.

B. Initial positron temperature

Shown in Figs. 4(a) and 4(b) are the standard deviations of the energy and time distributions obtained using a variety of initial temperatures, T_0 , with all other parameters as in Fig. 1. As seen in Fig. 4(a), σ_{\parallel} increases by a factor of \sim 5 as T_0 is increased from 5 to 500 K, but becomes quite insensitive to temperature as T_0 is increased further. In contrast, the temporal spread is seen to increase rapidly with T_0 at low temperatures, then asymptotes to approximately $\sigma_{\tau} \propto T_0$ at high temperatures.

To better illustrate the effect of temperature on the available particle trajectories, the final and initial parallel energies of the particles which are ejected with the lowest and highest final parallel energies in the beam are shown in Figs. 4(c)

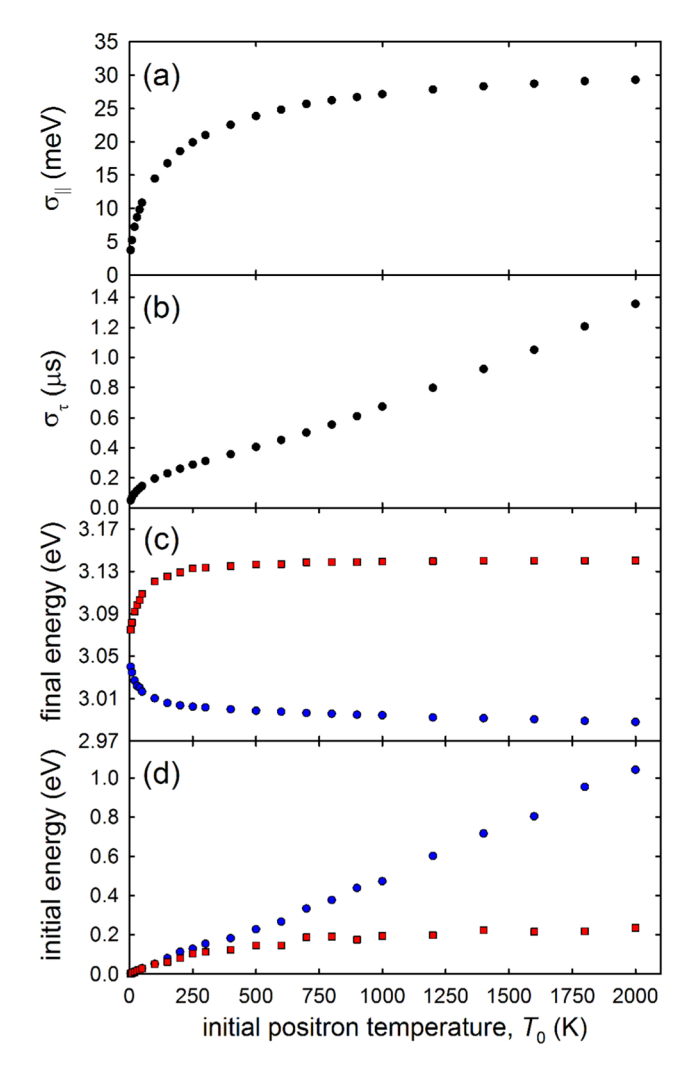


FIG. 4. Standard deviations of the (a) parallel energy and (b) temporal distributions of beams generated using various initial particle temperatures. Also shown is the (c) final and (d) initial parallel energies of the particles which are ejected with the (\bullet) lowest and (\blacksquare) highest final parallel energies in the beam. All other parameters as in Fig. 1.

and 4(d). Here it is seen that the final energies of both of the extreme energy particles are relatively constant at high temperatures, while at low temperatures the minimum energy increases and the maximum energy decreases, resulting in a relatively rapid narrowing of the full width of the parallel energy distribution.

In contrast, as seen in Fig. 4(d), the initial energies of both the lowest and highest final energy particles are "selected" from specific energies in the initial thermal distribution. The particle ejected with the lowest final energy is on the high energy tail of the initial thermal distribution, and increases proportionately to the initial temperature with an energy $\sim 6k_bT_0$. At high temperatures, the particle ejected with the highest final energy is one which has an initial parallel energy much lower in the thermal distribution. This optimal energy, which corresponds to an optimal width in the well and therefore an optimal final reflection position on the exit-gate potential, is relatively constant as the temperature is decreased until the temperature is low enough that this initial energy state is no-longer populated, at which point both the lowest and highest final energy particles are selected from the tail of the initial thermal distribution.

In light of the discussion above, the effects of the particle temperature on the beam distributions may be summarized as follows. At high temperatures, the initial phase-space is sufficiently populated that the optimal well width may be obtained, and so all trajectories described by Eq. (4) with $0 \le t_E - t_U \le \tau_f$ are available. This is the full bounce regime. The primary effect of increasing the temperature in this regime is that particles on the tail of the initial thermal distribution are able to escape the trap at earlier times when $V_W < V_E$, leading to an approximately linear relationship between σ_{τ} and T_0 at high temperatures (as seen in Fig. 4(b)). Because of the presence of the exit-gate barrier, those particles which escape the trap at earlier times are still ejected with approximately the minimum possible energy, $E_{\parallel} \sim e \phi_E$, while the particle ejected with the highest energy is the one which makes a full bounce above the exit-gate potential and therefore is ejected with the maximum possible energy, $E_{\parallel} \sim e \phi_E + \tau_f^h V_W$. Since the extreme particles are approximately at their minimum and maximum possible values in this regime, the temperature has little effect on their ejection trajectories, resulting in σ_{\parallel} becoming insensitive to T_0 at higher temperatures (as seen in Fig. 4(a)).

As the temperature is decreased the particles obtain sufficient energy to escape the trap at later times in the ejection process, resulting in a reduction in σ_{τ} . At very low temperatures the smaller initial phase-space results in the particles being unable to escape the trap until $V_W \approx V_E$ and the potential is nearly flat. Here, the possible ejection trajectories are constrained to those where $0 \ll t_E - t_U \ll \tau_f$. This is the low temperature regime. In this regime the possible extreme energy trajectories are both set by particles on the tail of the initial energy distribution, resulting in a relatively strong reduction in both energy and temporal spreads as the temperature is reduced.

In contrast, in the non-dynamic regime $\sigma_{\parallel} \approx 1/2k_bT_0$, assuming the final potential is relatively flat over the regions the particles occupy. For this reason, at high temperatures

superior energy spread is obtained by operating in the dynamic regimes discussed above; however, at low temperatures operating in the non-dynamic regime may yield lower parallel energy spreads.

C. Well depth

Shown in Fig. 5 are data for σ_{\parallel} and σ_{τ} when the initial well depth, defined here as $D_W \equiv V_E - V_W(0)$, is adjusted by varying the initial voltage applied to the well electrode, $V_W(0)$. Here, it is seen that increasing the well depth from 1 V to 50 V provides a \sim 75% improvement in parallel energy spread and a factor of two improvement in σ_{τ} , with the improvements becoming less significant as the well depth is increased above $D_W \sim$ 50 V. These improvements are due to an increase in the amount of adiabatic cooling undergone during ejection.

The time dependence of the potential well width and particle parallel temperature is shown in Fig. 6 for initial well depths of 1, 3, 10, and 50 V. As discussed in Ref. I, the existence of a longitudinal adiabatic invariant for this system requires that the product of the parallel velocity of the particles and the spatial width of the potential well be constant, therefore as the well width increases during ejection the particle parallel velocities must decrease. The amount of adiabatic cooling is proportional to the square of the ratio of the initial to final well widths (cf. Ref. I, Eq. (21)), and so the particles confined in a deeper (narrower) initial well cool to a lower final parallel temperature T_f before ejection, as seen

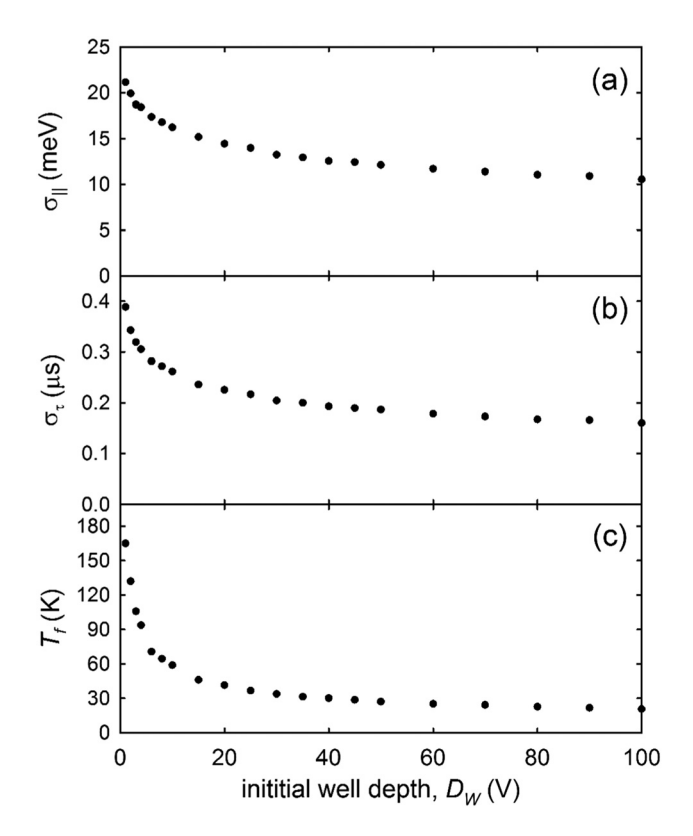


FIG. 5. Standard deviation of the (a) parallel energy and (b) temporal distributions using a variety of initial well depths, $D_W \equiv V_E - V_W(0)$. Also shown in (c) is the final parallel temperature, T_f . All other parameters as in Fig. 1.

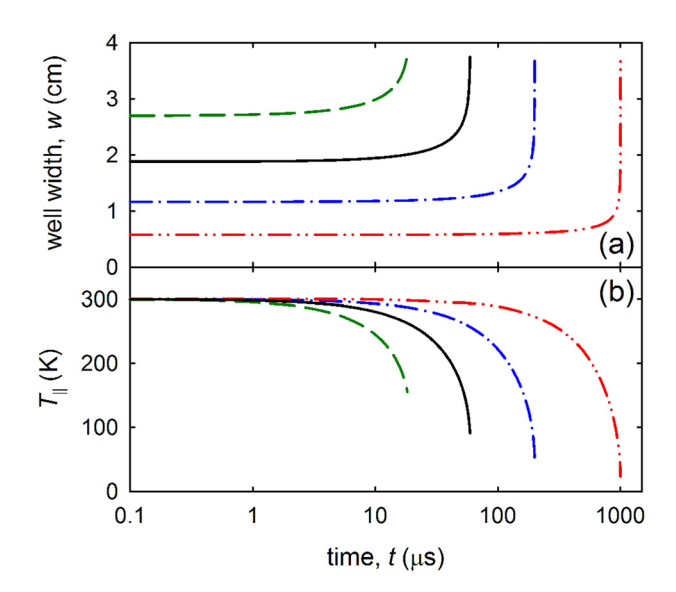


FIG. 6. (a) Average potential well width as seen by the particles and (b) particle parallel temperature as a function of time using an initial well depth of (--) 1 V, (--) 3 V, $(-\cdot-)$ 10 V and $(-\cdot-)$ 50 V.

in Fig. 5(c), thus yielding improvements to both σ_{\parallel} and σ_{τ} via the temperature effects described in Sec. V B.

In order for adiabatic cooling to occur, beam formation times must be fast compared to positron-neutral collision times. These collisions would result in positron-neutral rethermalization of the parallel energy distribution during ejection, and consequently both the parallel energy and temporal spreads would be larger than in the collision-free case described here.

In the non-dynamic regime, the particles are ejected sufficiently fast that axial motion is negligible during beam formation, and thus no adiabatic cooling occurs. In this case, increasing the well depth does not directly affect the resulting energy distribution. However, deeper (narrower) initial potential wells reduce the axial extent of the positron cloud, thereby reducing the region over which a flat final potential must be maintained in order for the ejection process to leave the parallel energy distribution unaltered (i.e., $\sigma_{\parallel} = 1/2k_bT_0$).

D. Trap geometry

The trap geometry, as parameterized by the length L and aspect ratio $\alpha \equiv L/D$ of the respective electrodes, plays an important role in beam performance. Here, the lengths of both the exit-gate and well electrode are independently varied in order to examine the effect the trap geometry has on beam quality. Since the electrode diameter is held constant $(D=8\,\mathrm{cm})$, the aspect ratio also varies with the length. For small aspect ratios the on-axis potential is approximately parabolic with a peak in potential less than the applied voltage. As α is increased, the ratio of the peak potential to the applied potential approaches unity, with the potential becoming flat near the axial center of the electrode.

Shown in Figs. 7(a) and 7(b) are σ_{\parallel} and σ_{τ} obtained using various lengths for the exit-gate electrode L_E . Here it is seen that both σ_{\parallel} and σ_{τ} are relatively insensitive to L_E at larger lengths and aspect ratios, however for aspect ratios $\alpha_E \leq 1$ both spreads increase as L_E is reduced. As discussed

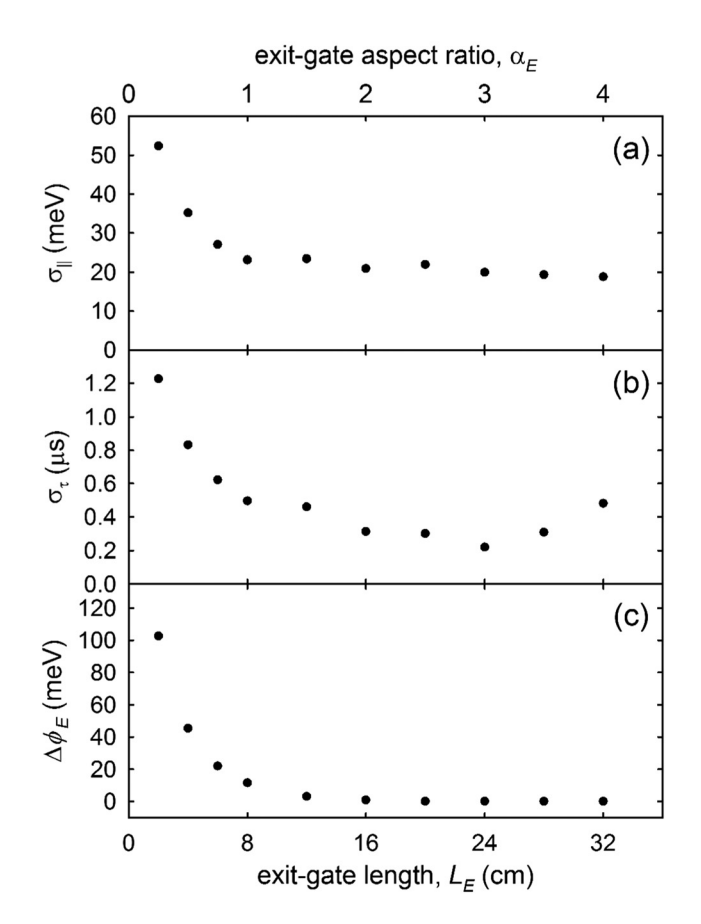


FIG. 7. Standard deviation of the (a) parallel energy and (b) time distributions of beams produced by traps with a variety of exit-gate electrode lengths. Also shown in (c) is the change in magnitude of the peak in exit-gate potential during particle ejection. All other parameters as in Fig. 1.

above, the peak in the exit-gate potential sets the minimum possible parallel energy of any particle in the beam, $E_{\parallel} \gtrsim e\phi_E$, as well as the minimum time at which a particle may escape the trap. At small aspect ratios $\phi_E < V_E$, and so as the potential applied to the adjacent well electrode is increased to eject the particles, there is a corresponding increase in ϕ_E (i.e., the effective aspect ratio of the exit-gate electrode is increased as V_W approaches V_E). This results in a time-dependent increase in the magnitude of the exit-gate barrier during the time the particles are ejected, as shown in Fig. 7(c), thus leading to an increase in both the parallel energy and time spreads of beams produced using small values of α_E .

While σ_{\parallel} is approximately flat at $\alpha_E \gtrsim 1$, σ_{τ} continues to have a weak dependence on L_E , as seen in Fig. 7(b). As L_E is increased, the time over the exit barrier becomes comparable to the time required to eject the remaining particles. This, in turn, allows later-ejected particles to partially catch up with earlier ones, thus further reducing σ_{τ} . As L_E is increased, the time required for the earlier (low energy) particles to cross the exit-gate barrier becomes sufficiently long for them to be overtaken by the later-released (higher energy) particles, leading to an increase in σ_{τ} . This effect is more dramatic for beams generated using higher ramp rates (not shown).

The effects of the well electrode length L_W on σ_{\parallel} and σ_{τ} are shown in Figs. 8(a) and 8(b). In this case both spreads increase significantly as L_W is increased, with σ_{\parallel} increasing

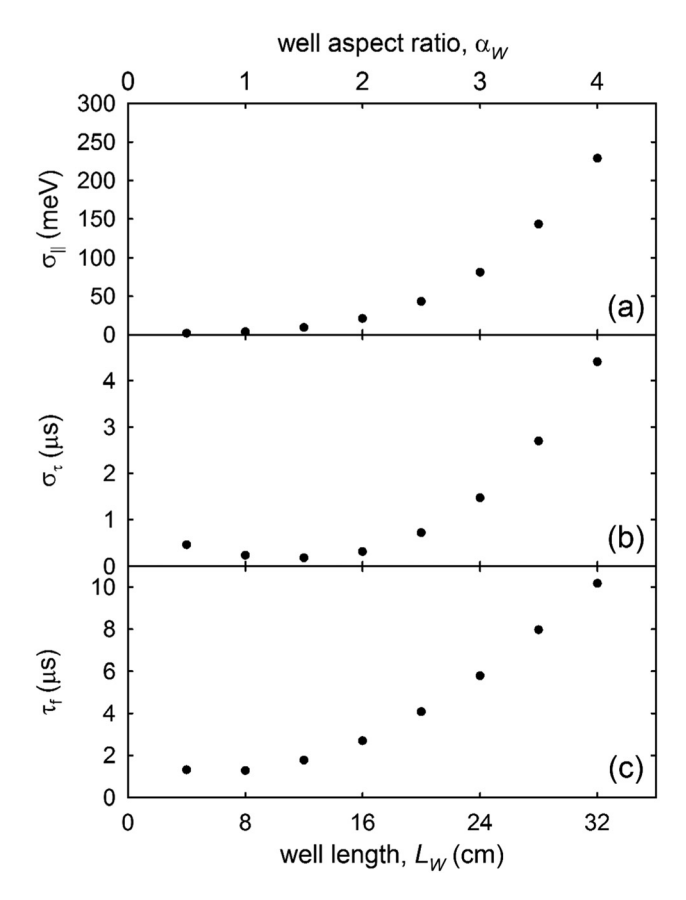


FIG. 8. Standard deviation of the (a) parallel energy and (b) time distributions of beams produced by traps with a variety of well electrode lengths. Also shown in (c) is the average final bounce time during particle ejection. All other parameters as in Fig. 1.

by more than a factor of 130 between $L_W = 4$ cm and 32 cm. This strong dependence on L_W is due to the effect the width and shape of the potential well has on the particle axial bounce times.

Shown in Fig. 8(c) is the mean time required for the particles to make their final axial bounce within the well, $\bar{\tau}_f$. Here it is seen that $\bar{\tau}_f$ increases significantly as L_W is increased, and in a similar manner to both σ_{\parallel} and σ_{τ} . At small values of α_W , the well potential is relatively parabolic, and so the bounce time is less sensitive to changes in L_W in this regime. However, for values of $\alpha_W \gtrsim 2$, where the potential well is relatively flat, increasing L_W leads to a rapid increase in the bounce times of the particles.

As discussed above, the time spread is largely set by the time required for the particles to overcome the exit-gate barrier and be ejected from the trap, while the parallel energy spread is predominantly set by the change in energy imparted to the particles during their last bounce, and so both processes are sensitive to $\bar{\tau}_f$.

It should also be noted that here both the beam and electrode diameters are held constant at 0.5 cm FWHM and 8 cm, respectively. Under these conditions radial effects due to gradients in the axial potential are small and do not contribute significantly to the energy and time spreads of the resulting beam. However, in cases where the ratio of the beam diameter to the electrode diameter is close to unity the radial effects introduced by using small aspect ratio

electrodes will begin to lead to a broadening of the energy and temporal spreads.

E. Shape of beam distributions

While the impact of the beam formation conditions on the spreads in the parallel energy and time distributions has been presented, it is also of interest to examine how these conditions effect the *shape* of the distributions. Shown in Fig. 9 are the beam distributions obtained under three qualitatively different conditions. Figures 9(a) and 9(b) show the distributions for a typical beam formation protocol using a roughly parabolic potential well and typical ramp rate: $V_T = 5 \text{ V}$, $V_E = 3 \text{ V}$, $V_0 = 0 \text{ V}$, and $\dot{V}_W = 50 \text{ mV}/\mu\text{s}$, with aspect ratios 2, 1, and 2 for the trapping, well and exit-gate electrodes, respectively. Under these conditions, both the parallel energy and time distributions can be roughly described as Gaussian and thus described by the detailed analysis presented in Ref. I.

Shown in Figs. 9(c) and 9(d) are the distributions using the same parameters as that of (a) and (b), but with the well aspect ratio increased from 1 to 4, resulting in a long flat trapping well. In this case, both the energy and time distributions deviate significantly from Gaussians. This suggests an important conclusion that Gaussian-like distributions are associated with potential wells that are (roughly) parabolic in shape.

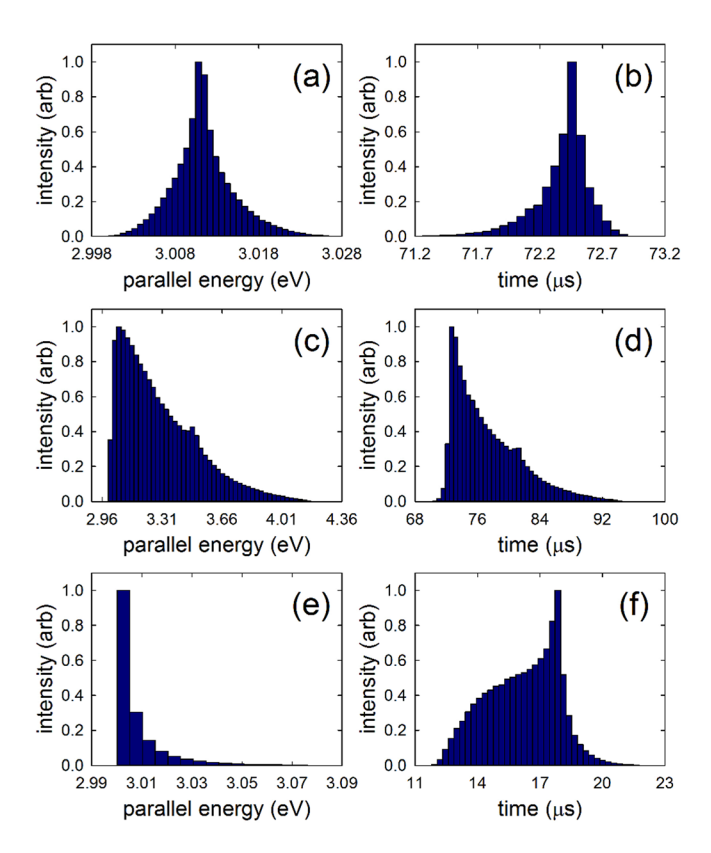


FIG. 9. (left) Parallel energy and (right) temporal distributions for three specific trapping geometries and ejection protocols: (a) and (b) typical parabolic potential well and ejection protocol; (c) and (d) long flat potential well and typical ejection protocol; and (e) and (f) typical parabolic potential well with ultra-fast ejection protocol. The σ_{\parallel} values for (a), (c), and (e) are 3.7, 223, and 12.6 meV, respectively; and the corresponding σ_{τ} values are 0.23, 4.3, and 1.7 μ s. See text for details.

Shown in Figs. 9(e) and 9(f) are the distributions for the case of an ultra-fast release, putting beam formation in the non-dynamic regime. The parameters are $V_T = 3.3 \, \mathrm{V}$ and $V_E = 3 \, \mathrm{V}$, with the well voltage increased linearly from 0 to $3 \, \mathrm{V}$ in $0.1 \, \mu \mathrm{s}$, using electrodes with aspect ratios $\alpha = 2$. While the initial well is approximately parabolic, the final potential is reached on time scales fast compared to the axial bounce time, and so adiabatic cooling does not occur and the initial parallel energy distribution is unaltered by the presence of the exit-gate barrier. Further, provided the final potential is reasonably flat over the region the particles occupy, particles are ejected from the trap with their initial thermal velocities plus their potential relative to ground. Under these conditions, the parallel energy distribution is a shifted Maxwell-Boltzmann distribution with $\sigma_{\parallel} = 1/2k_bT_0$.

VI. SUMMARY AND CONCLUSIONS

Simulation results have been presented for pulsed, magnetically guided positron beams formed using generic Penning-Malmberg-style traps in a uniform magnetic field. This study elucidates the process of beam formation, especially concerning its impact on beam quality. This understanding is used, in turn, to find optimum conditions for beam formation, with emphasis on situations in which a low energy spread beam is desired, delivered in pulses of microsecond duration or shorter. These results showed three distinct regimes in which beam formation occurs; the full bounce and low temperature dynamic regimes, and the fast ejection non-dynamic regime.

A general description of the processes undergone during beam formation in the two dynamic regimes may be summarized as follows. As the well voltage is increased to eject the particles, the well width increases. This results in a decrease in the parallel temperature (due to adiabatic cooling) and an increase in the axial bounce time. The particles are first able to escape the trap when the sum of their kinetic and potential energy exceeds the peak in the exit-gate potential.

In the full bounce regime, the first particles to escape are those on the high energy tail of the initial thermal distribution which gain sufficient energy to overcome the exit-gate barrier at the end of their final bounce cycle and are therefore ejected with the minimum parallel energy, while the final particles to leave are those which obtain sufficient energy to escape at the beginning of their final bounce cycle, and are therefore required to make a full pass through the rising potential region above the exit-gate potential and so are ejected with the maximum parallel energy.

In contrast, in the low temperature regime none of the particles are able to explore far enough in the well to escape the trap unaffected by the rising potential or to reach the optimal reflection point on the exit-gate for their final bounce. Here both the first and last particles to escape are those on the tail of the initial thermal distribution that are moving towards and away from the exit-gate barrier, respectively, as they obtain sufficient energy to escape the trap. This results in a raising of the minimum and a lowering of

the maximum possible final parallel energies, thus resulting in improved temporal and energy spreads of the beam.

The resulting beam quality obtained under a variety of conditions was also discussed. It was shown that the average ramp rate during the time the particles escape the trap is a critical parameter and that the detailed time dependence of the ramp at earlier times is not important. Large ramp rates cause the particles to be accelerated out of the trap more quickly, and to higher energies, than low ramp rates. It was also shown that both the parallel energy and time spread improve as the temperature is reduced. This effect is due to the reduction of phase-space at low temperatures, which leads to a restriction on the possible extreme trajectories, and therefore results in narrower energy and time distributions. Since reducing the positron temperature also decreases the perpendicular energy spread, this provides a very effective method of improving the total energy spread of the beam, provided the parallel energy spread (set by the other dynamics during beam formation) does not dominate over the perpendicular spread.

The effects of the potential well depth and trap geometry were also shown to effect beam quality. Here it was seen that the amount of adiabatic cooling during ejection could be increased by increasing the initial well depth and therefore decreasing the initial well width. Additionally, it was shown that narrow, parabolic potential wells result in shorter positron bounce times, which improves both the energy and temporal spreads of the resulting beam. Finally, compact Gaussian-like parallel energy and time distributions can be produced using approximately parabolic trapping potential wells and moderate ramp rates.

Using the results presented here, optimal trap geometry and ejection parameters for producing beams with low energy spreads and reasonable temporal spreads may be described. An ideal trap geometry will have exit-gate and well aspect ratios of $\alpha_E \gtrsim 1$ and $\alpha_W \lesssim 1$, respectively, while maintaining the shortest lengths possible. The voltage applied to the well electrode should be made small compared to the voltage applied to the exit-gate electrode to ensure the positrons are trapped within a narrow parabolic potential well, and the positrons should be cooled to the lowest possible temperature before beam formation begins. The positrons should then be ejected by increasing the well voltage at the lowest possible rate which still yields satisfactory temporal spreads for the desired application.

The study of low-energy positron-matter interactions is currently limited by beam quality. It is hoped that the more detailed knowledge of the processes operative in beam formation and their effects on beam quality provided by this study will lead to the development of improved beams, and therefore enable a new generation of high-precision studies.

As a start on this development path, the results presented here and in Refs. 20 and 23 were used to design, construct, and test a new positron trap. This new device re-traps positrons ejected from a 300 K buffer gas trap, compresses them both radially and axially, and cools them to $\sim 50 \, \text{K}$ through interactions with a cryogenically cooled buffer gas. ²⁴ Using this technique, positron beams with *total* energy spreads of $\Delta E_t = 6.9 \pm 0.7 \, \text{meV}$ FWHM ($\sigma_t = 4.8 \pm 0.3 \, \text{meV}$) have been

produced, which is a factor of \sim 5 improvement over the previous state-of-the-art, while maintaining sub-microsecond temporal spreads and beams diameters as small as 1 mm.

ACKNOWLEDGMENTS

This work was supported by the U.S. National Science Foundation, Grant No. PHY 14-01794.

¹G. F. Gribakin, J. A. Young, and C. M. Surko, Rev. Mod. Phys. **82**, 2557 (2010).

²N. Guessoum, P. Jean, and W. Gillard, Mon. Not. R. Astron. Soc. **402**, 1171 (2010).

³Principles and Practice of Positron Emission Tomography, edited by R. L. Wahl (Lippincott Williams & Wilkins, Philadelphia, PA, 2002).

⁴D. W. Gidley, H.-G. Peng, and R. S. Vallery, Annu. Rev. Mater. Sci. 36, 49 (2006)

⁵G. B. Andresen, M. D. Ashkezari, M. Baquero-Ruiz, W. Bertsche, P. D. Bowe, E. Butler, P. T. Carpenter, C. L. Cesar, S. Chapman, M. Charlton, J. Fajans, T. Friesen, M. C. Fujiwara, D. R. Gill, J. S. Hangst, W. N. Hardy, M. E. Hayden, A. J. Humphries, J. L. Hurt, R. Hydomako, S. Jonsell, N. Madsen, S. Menary, P. Nolan, K. Olchanski, A. Olin, A. Povilus, P. Pusa, F. Robicheaux, E. Sarid, D. M. Silveira, C. So, J. W. Storey, R. I. Thompson, D. P. van der Werf, J. S. Wurtele, and Y. Yamazaki (ALPHA Collaboration), Phys. Rev. Lett. 106, 025002 (2011).

⁶J. R. Danielson, T. R. Weber, and C. M. Surko, Appl. Phys. Lett. **90**, 081503 (2007).

⁷T. R. Weber, J. R. Danielson, and C. M. Surko, Phys. Plasmas **16**, 057105 (2009).

⁸T. R. Weber, J. R. Danielson, and C. M. Surko, Phys. Plasmas 17, 123507 (2010).

⁹N. C. Hurst, J. R. Danielson, and C. M. Surko, Phys. Plasmas **22**, 073503 (2015).

¹⁰T. J. Murphy and C. M. Surko, Phys. Rev. A **46**, 5696 (1992).

¹¹S. J. Gilbert, C. Kurz, R. G. Greaves, and C. M. Surko, Appl. Phys. Lett. 70, 1944 (1997).

¹²M. Amoretti, C. Amsler, G. Bonomi, A. Bouchta, P. Bowe, C. Carraro, C. L. Cesar, M. Charlton, M. J. T. Collier, M. Doser, V. Filippini, K. S. Fine, A. Fontana, M. C. Fujiwara, R. Funakoshi, P. Genova, J. S. Hangst, R. S. Hayano, M. H. Holzscheiter, L. V. Jorgensen, V. Lagomarsino, R. Landua, D. Lindelof, E. L. Rizzini, M. Macri, N. Madsen, G. Manuzio, M. Marchesotti, P. Montagna, H. Pruys, C. Regenfus, P. Riedler, J. Rochet, A. Rotondi, G. Rouleau, G. Testera, A. Variola, T. L. Watson, and D. P. van der Werf, Nature 419, 456 (2002).

¹³G. Gabrielse, N. S. Bowden, P. Oxley, A. Speck, C. H. Storry, J. N. Tan, M. Wessels, D. Grzonka, W. Oelert, G. Schepers, T. Sefzick, J. Walz, H. Pittner, T. W. Hänsch, and E. A. Hessels (ATRAP Collaboration), Phys. Rev. Lett. 89, 213401 (2002).

¹⁴G. B. Andresen, M. D. Ashkezari, M. Baquero-Ruiz, W. Bertsche, P. D. Bowe, E. Butler, C. L. Cesar, S. Chapman, M. Charlton, A. Deller, S. Eriksson, J. Fajans, T. Friesen, M. C. Fujiwara, D. R. Gill, A. Gutierrez, J. S. Hangst, W. N. Hardy, M. E. Hayden, A. J. Humphries, R. Hydomako, M. J. Jenkins, S. Jonsell, L. V. Jorgensen, L. Kurchaninov, N. Madsen, S. Menary, P. Nolan, K. Olchanski, A. Olin, A. Povilus, P. Pusa, F. Robicheaux, E. Sarid, S. S. e. Nasr, D. M. Silveira, C. So, J. W. Storey, R. I. Thompson, D. P. van der Werf, J. S. Wurtele, and Y. Yamazaki, Nature 468, 673 (2010).

¹⁵G. Gabrielse, R. Kalra, W. S. Kolthammer, R. McConnell, P. Richerme, D. Grzonka, W. Oelert, T. Sefzick, M. Zielinski, D. W. Fitzakerley, M. C. George, E. A. Hessels, C. H. Storry, M. Weel, A. Müllers, and J. Walz (ATRAP Collaboration), Phys. Rev. Lett. 108, 113002 (2012).

¹⁶D. B. Cassidy and A. P. Mills, Nature **449**, 195 (2007).

¹⁷D. Chaudhary, M. Went, K. Nakagawa, S. Buckman, and J. Sullivan, Mater. Lett. **64**, 2635 (2010).

 M. Surko, G. F. Gribakin, and S. J. Buckman, J. Phys. B 38, R57 (2005).
 C. Kurz, S. Gilbert, R. Greaves, and C. Surko, Nucl. Instrum. Methods Phys. Res., Sect. B 143, 188 (1998).

²⁰M. Natisin, J. Danielson, and C. Surko, Phys. Plasmas **22**, 033501 (2015).

²¹G. F. Gribakin and C. M. R. Lee, Phys. Rev. Lett. **97**, 193201 (2006).

²²H. Goldstein, *Classical Mechanics* (Addison Wesley, 1980).

²³M. Natisin, J. Danielson, and C. Surko, J. Phys. B 47, 225209 (2014).

²⁴M. R. Natisin, J. R. Danielson, and C. M. Surko, App. Phys. Lett. 108, 024102 (2016).